ACS APPLIED NANO MATERIALS

www.acsanm.org Article

Robust Nanocapacitors Based on Wafer-Scale Single-Crystal Hexagonal Boron Nitride Monolayer Films

Yanwei He, Yuan Li, Miguel Isarraraz, Pedro Pena, Jason Tran, Long Xu, Hao Tian, Tianchen Yang, Peng Wei, Cengiz S. Ozkan, Mihrimah Ozkan, and Jianlin Liu*

Cite This: ACS Appl. Nano Mater. 2021, 4, 5685−5695 Read Online

ACCESS | Metrics & More | Article Recommendations | Supporting Information

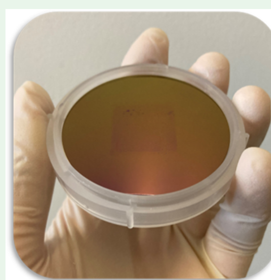

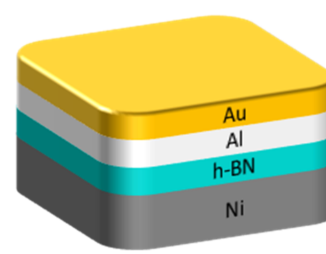

ABSTRACT: Two-dimensional wafer-scale and single-crystal hexagonal boron nitride (h-BN) films are considered a crucial part of the next generation of van der Waals (vdW) electronic devices. Progress has been made in the synthesis process recently, leading to the demonstration of electronic devices. In this work, we report an effective method to synthesize high-quality single-crystal h-BN monolayer films. Single-crystal metal substrates were produced by thermal annealing of Ni foils, followed by electropolishing to remove the passivated surface layer. Molecular beam epitaxy was employed to synthesize 1 in.^{2} monolayer single-crystal h-BN films. We discovered that electropolishing plays an important role in drastically increasing the speed of h-BN film growth. Robust nanocapacitors were fabricated using as-grown monolayer h-BN films. The nanocapacitance effect and tunneling current mechanism were studied in detail, and the "effective distance" concept is introduced to explain the quantum phenomenon in the (vdW) metal−insulator−metal devices using atomically thin dielectric h-BN films.

KEYWORDS: *hexagonal boron nitride, single crystal, nanocapacitor, molecular beam epitaxy, two dimensional*

Downloaded via UNIV OF CALIFORNIA RIVERSIDE on July 12, 2021 at 19:34:27 (UTC).
See https://pubs.acs.org/sharingguidelines for options on how to legitimately share published articles.

1. INTRODUCTION

Two-dimensional (2D) hexagonal boron nitride (h-BN) materials and their applications in vast areas have been at the forefront of 2D materials research for the last two decades. Their wide band gap (5.9 eV), high breakdown electric field (12 MV/cm),[1] and dangling bond-free surface render them a perfect insulating layer, especially for van der Waals (vdW) devices. Exfoliated h-BN flakes have been widely used in tunneling devices, field-effect transistors, and capacitors.[2−4] In contrast, h-BN films obtained from bottom-up synthesis such as chemical vapor deposition (CVD) and molecular beam epitaxy (MBE) possess larger defect density compared to exfoliated single-crystal flakes. The defects in h-BN films, such as grain boundaries, have been utilized in resistive switching memory devices[5,6] and are also promising for single-photon emitter devices.[7] However, when their insulating properties are needed, h-BN films with a larger density of defects would exhibit a large leakage current, which essentially degrades the performance of the devices. Thus, it is critical to enhance the quality of the h-BN films for these applications.

One way to reduce and diminish the defect density is to grow high-quality single-crystal h-BN films. Lee et al. achieved the growth of wafer-scale single-crystal h-BN films by utilizing the self-collimation of h-BN flakes on a melted Au surface.[8] Wang et al. adopted another method, step edge-enhanced epitaxy, by taking advantage of step edges on a Cu(110) surface.[9] Similarly, Chen et al. reported the step edge-enhanced epitaxial growth of wafer-scale single-crystal h-BN on the single-crystal Cu(111) substrate.[10] However, such methods to obtain single-crystal metal substrates for h-BN growth are rather sophisticated. In the case of using metal films obtained from deposition as substrates, desorption and surface pitting during annealing were observed.[11,12] Another issue is that even though wafer-scale single-crystal h-BN films were reported, electrical devices were rarely fabricated. Chen et al. reported that the metal−insulator−metal (MIM) devices comprising (Ti/h-BN/Cu) layers on polycrystal monolayer h-BN films are almost conductive, while those on single-crystal monolayer h-BN films have a small breakdown voltage at 0.1 V.[10] In contrast, the breakdown voltage of MIM devices with Ni and Co as electrodes on our MBE-grown monolayer h-BN films is around 0.8 V, indicating higher film quality.[13−15] One issue in these h-BN samples is the long growth time required to obtain a continuous h-BN film, which is not efficient.

Received: February 1, 2021
Accepted: May 18, 2021
Published: June 1, 2021

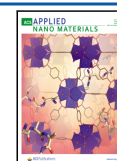

© 2021 American Chemical Society

https://doi.org/10.1021/acsanm.1c00298
ACS Appl. Nano Mater. 2021, 4, 5685−5695

Scheme 1. Experimental Schematic for the Growth of the H-BN Film

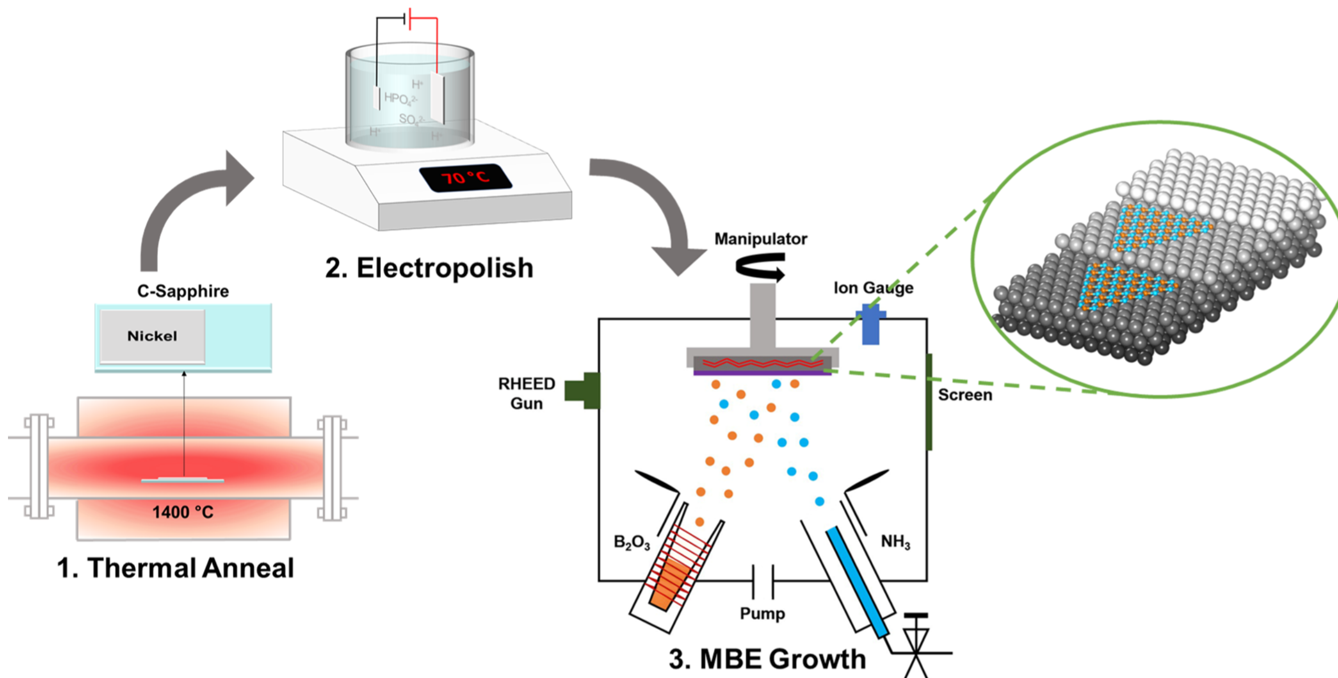

The second way to ensure the quality of the h-BN film is to minimize the process-induced defects during device fabrication. "High-energy" atom or cluster evaporated from the hot metal surface in a vacuum chamber for metal contacts to the material has been known to damage the targeted surfaces by physical bombardment or strong local heating.[16,17] For multilayer films, a little damage on the surface layer may not become an issue,[18,19] but for single-layer films, the same damage can cause the entire film to be leaky electrically. Efforts have been made to address this problem. For example, to prevent damage of MoS_2 from heavy transition metals, Kim et al. employed low-thermal-energy evaporation deposition of indium,[20] and Liu et al. replaced metal deposition with the electrode transfer technique.[17] In the fabrication of molecular electronic devices, an indirect deposition technique was adopted to avoid damage from direct atomic beams.[21,22]

This work aims to address the problems mentioned above. Many methods such as MBE,[23] CVD,[24] atomic layer deposition,[25] and solution-processed fabrication[26,27] have been adopted to obtain large-area h-BN films. Among these tools, MBE with precise control of growth parameters is an excellent candidate for epitaxial growth of high-quality films with atomic layer thicknesses, and thus, it is employed for h-BN growth in this project. Single-crystal substrates were obtained simply by thermal annealing of Ni foils. Different from thin metal films obtained by metal deposition techniques, post-annealed Ni foils can be further polished to keep the metal surface fresh and flat. By replacing mechanical polishing with electropolishing in this effort, we discovered that the h-BN nucleation density and the growth speed are drastically increased. Robust nanocapacitors were fabricated on as-grown h-BN films using "low-energy" Al atoms from a Temescal BJD 1800 e-beam evaporator to mitigate the process-induced damage effects on the films. The growth mechanism and film quality were also studied with scanning electron microscopy (SEM), scanning tunneling microscopy (STM), reflection high-energy electron diffraction (RHEED), atomic force microscopy (AFM), X-ray photoelectron spectroscopy (XPS), Raman spectroscopy, and ultraviolet−visible absorption spectroscopy (UV−Vis). The "effective distance" between two electrodes was extracted from capacitance analysis. The tunneling currents were measured and analyzed.

2. EXPERIMENTAL SECTION

2.1. Growth and Characterization. The growth procedure is summarized in Scheme 1. The as-received polycrystal Ni foil was first annealed to form (111) single crystal substrates and then electropolished and cleaned. The detailed procedure for substrate preparation is summarized in Figure S1 in the Supporting Information. A PerkinElmer MBE system with a background pressure of $\sim 10^{-9}$ Torr was employed for h-BN growth on the electropolished (111) substrate. B_2O_3 powder (Alfa Aesar, 99.999% purity) was used as the B source, and the effusion cell temperature was maintained at 1170 °C. Ammonia gas (American Gas Group, 99.9995% purity) was used as the N source, and the flow rate was maintained at 10 sccm. The substrate temperature for time-dependent growth was maintained at 867 °C. The secondary electron SEM images and electron backscattered diffraction (EBSD) images were acquired using an FEI NNS450 system. X-ray diffraction (XRD) spectra were acquired using a Panalytical Empyrean Series 2 system, and the XPS spectra were acquired using a Kratos AXIS ULTRA XPS system. The Raman spectra were obtained using a HORIBA LabRam system equipped with a 60 mW 532 nm green laser. AFM images were acquired using a tapping mode Veeco D5000 AFM system, and STM images were acquired using a tabletop NanoSTM. Please refer to our previous research for more information about the MBE growth procedures.[28,29] The RHEED experiment is carried out using a 15 keV electron beam with 7.5 mW beam energy.

2.2. Device Fabrication and Characterization. The capacitors were fabricated, following photolithography, metal deposition, and lift-off patterning. The metal contacts were deposited with an e-beam evaporator where a 20 nm thick Al layer was deposited at a rate of 0.2 Å/s, and a 100 nm thick Au layer was deposited at a rate of 1 Å/s. Electrical characterization of the devices was performed on a Signatone probe station, and the *I*−*V* measurements were acquired using an Agilent 4155C semiconductor parameter analyzer. Finally,

https://doi.org/10.1021/acsanm.1c00298
ACS Appl. Nano Mater. 2021, 4, 5685−5695

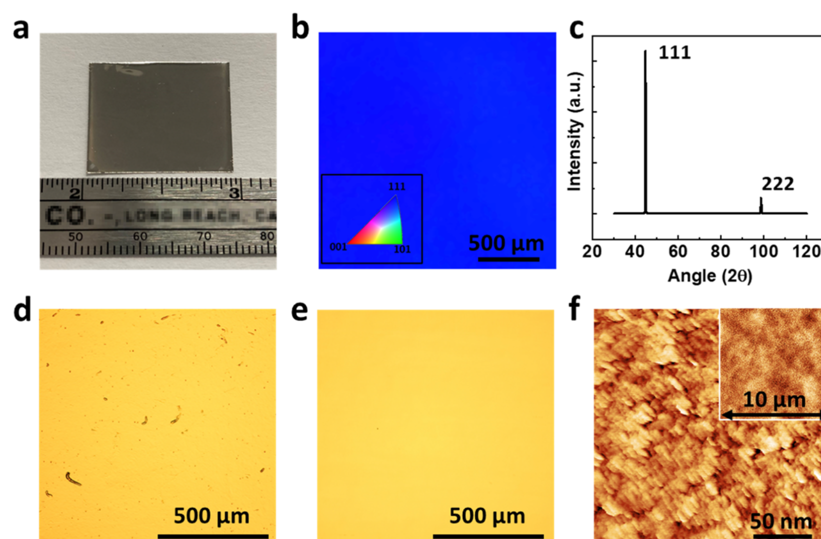

Figure 1. Characterization of the Ni(111) substrate. (a) Photograph of the 1 in.^{2} single crystal substrate obtained after thermal annealing; (b) EBSD IPF *Z* image showing the (111) surface direction; (c) XRD result showing the (111) surface direction; (d) photograph of the substrate before electropolishing; (e) photograph of the substrate after electropolishing; and (f) STM and AFM (inset) images of the substrate surface after electropolishing.

C−*V* and *C*−*f* measurements were acquired using a Keysight E4980A precision LCR meter.

3. RESULTS AND DISCUSSION

The as-received Ni foils (Alfa Aesar, 99.994%) were annealed in a ceramic tube furnace at 1400 °C for 90 min, resulting in (111) single-crystal surfaces. Figure 1a shows a photograph of the post-annealed 1 in.^{2} single-crystal substrate. There is a very small portion of polycrystal remaining in the lower left corner. The post-annealed substrate was then electropolished in a "H_2SO_4 + H_3PO_4" electrolyte mixture to remove the passivated surface layer formed during annealing and keeping the metal surface fresh and flat. The detailed substrate preparation procedures are illustrated in Figure S1. Figure 1b,c shows EBSD and XRD results, respectively. The blue color of the *Z*-direction inverse pole figure (IPF *Z*) and the diffraction peaks of XRD at 44.6 and 98.6° indicate that the surface orientation is (111). Figure 1d,e shows the photographs of substrates before and after electropolishing, respectively, demonstrating that the substrate surface after electropolishing is much smoother and cleaner. Figure 1f shows AFM and STM images of an electropolished substrate surface, where the root mean square roughness for a 10 μm^2 area is 0.5 nm. The STM image reveals that the nanoscale terraces and pits are formed on the metal surface after electrochemical reaction. XPS analysis was carried out, and the results are shown in Figure S2. No chemical residues are observed. In addition, the electro-polished substrate is more easily oxidized, which may indicate that the nanostructured surface is more chemically reactive. After the coverage of h-BN, no metal oxide-related XPS signals are observed, indicating a high-quality h-BN/substrate interface.

Figure 2a−d shows SEM images of samples after 10, 20, 30, and 40 min growth, respectively. Continuous films have been observed to form after 40 min growth. Figure 2e shows XPS spectra taken from a continuous h-BN film (Figure 2d). The sharp B_1s and N_1s signals are indicative of high film quality. Additional h-BN growth results are available in the Supporting Information section (Figure S3). Our recent article reported on the h-BN growth on mechanically polished Ni(111) substrates under similar growth conditions.[14] We have discovered that the growth speed on electropolished substrates is nearly 20 times faster compared to the growth speed on mechanically polished substrates.[14] The reason for this dramatic improvement could be the availability of many more h-BN nucleation sites obtained via electropolishing. As shown in Figure 1f, the nanoscale protrusions and pits formed by electrochemical reactions may evolve into favorable h-BN nucleation sites at the growth temperatures. Further evidence for this hypothesis is shown in Figure S4, where a dense array of h-BN nuclei has been observed on an uncovered metal surface in between the h-BN flakes. The time-dependent growth results reveal that the h-BN flakes are well aligned before merging, indicating a strong epitaxial growth relationship between h-BN and the Ni(111) surface. Figure 2f provides a summary of the edge direction distribution of h-BN flakes on the sample shown in Figure 2b. Three major peaks are separated by 60°, confirming a good level of unidirectionality of h-BN flakes, which has been considered to be the key to achieve high-quality single-crystal films.[9,10] This strongly suggests that the continuous film shown in Figure 2d has a single crystal structure.

The epitaxial relationship was studied using h-BN coverage-dependent RHEED analysis, as shown in Figure 2g. The RHEED patterns were obtained on samples with 0% (Ni substrate after annealing), 60% (sample shown in Figure 2b), and 100% (sample shown in Figure 2d) h-BN coverage. Only two sets of patterns were observed, and they were separated by 30°. The row labeled by 0° corresponds to the $\langle 1\bar{1}0 \rangle$ directions, and the row labeled as 30° corresponds to the $\langle 11\bar{2} \rangle$ directions. The lattice constants calculated based on the RHEED patterns are ∼4.37 Å for the $\langle 1\bar{1}0 \rangle$ directions and ∼2.52 Å for the $\langle 11\bar{2} \rangle$ directions. No differences in the lattice constants have been resolved between Ni(111) and h-BN. The RHEED patterns for the Ni(111) substrate are slightly dotty, which are attributed to oxidation after being exposed to air.[30] In addition, due to the surface corrugations after h-BN film growth,[14] the RHEED patterns obtained on h-BN films are

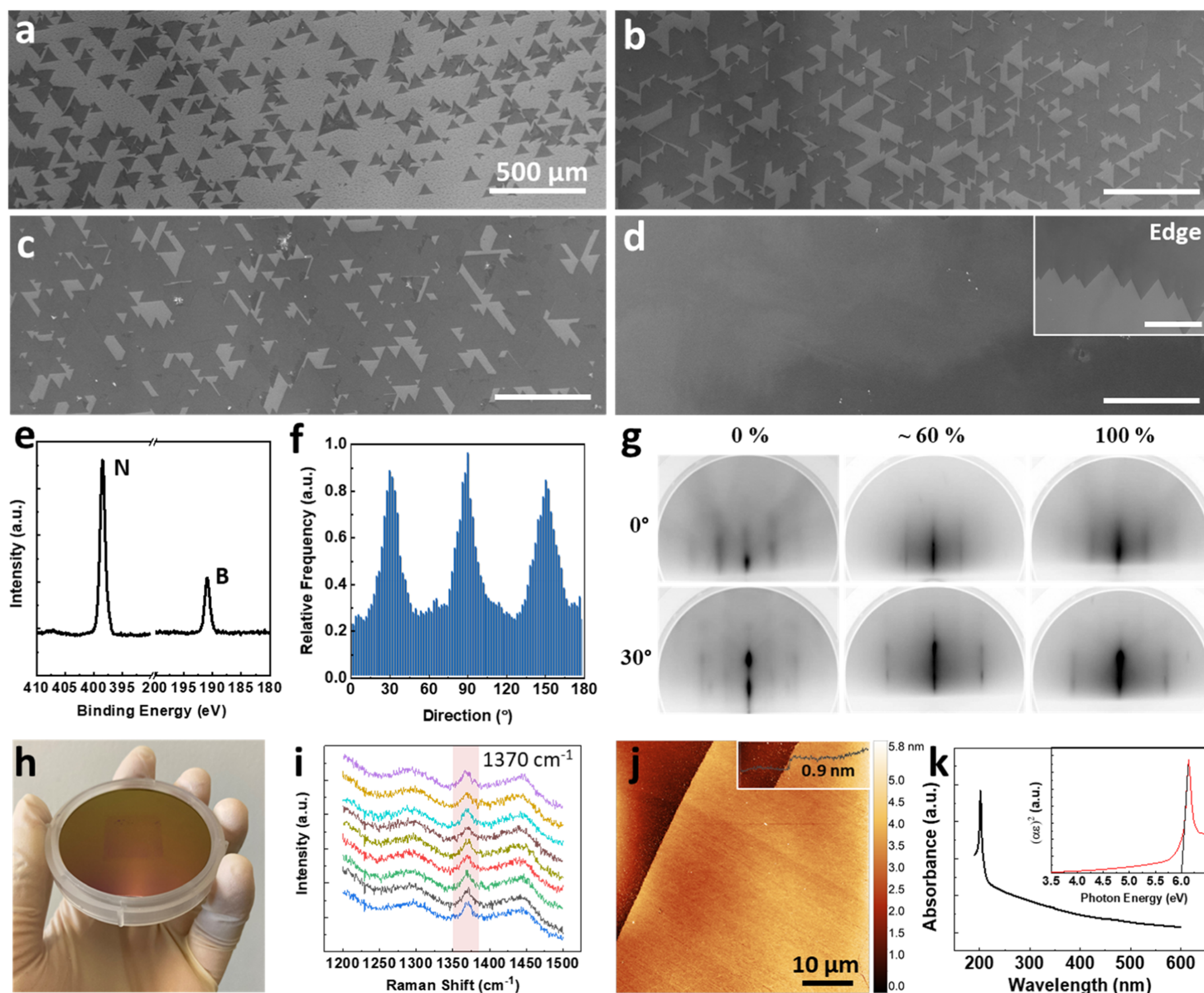

Figure 2. Characterization of h-BN grown on the Ni(111) single-crystal substrate. (a−d) SEM images of h-BN after growth for 10, 20, 30, and 40 min, respectively; an inset in d shows the image of the sample at the edge area. All scale bars are 500 μm; (e) XPS spectrum of the as-grown h-BN film shown in (d); (f) edge direction analysis of the sample shown in (b); (g) h-BN coverage-dependent RHEED analysis; (h) photograph of the h-BN film transferred on a 2 in. SiO_2/Si wafer; (i) Raman spectra taken on nine different areas on the transferred sample shown in (h); (j) AFM image taken on the transferred sample shown in (h); the inset shows a linear scan profile across the edge; and (k) UV−Vis absorption spectrum of a transferred h-BN sample on sapphire. The inset shows a Tauc plot.

also faint. Nevertheless, the coverage-dependent RHEED analysis confirms that there is no in-plane rotation between h-BN and the Ni(111) surface, further indicated by theoretical calculations.[31,32]

Figure 2h shows a photograph of a single-crystal h-BN film transferred onto a 2 in. diameter SiO_2/Si wafer. The detailed transfer process is available in our previous report.[33] The Raman spectra shown in Figure 2i are obtained from nine different spots on the transferred h-BN film. The h-BN peaks are located at around 1370 cm^{-1}, indicating a uniform single-layer h-BN film.[34] The other two peaks at 1293 and 1445 cm^{-1} are from the SiO_2/Si substrate.[35] The film thickness was further confirmed by AFM imaging, as shown in Figure 2j. The 50×50 μm^2 AFM image shows a clean and flat h-BN film after the transfer process. The film thickness obtained from a line profile scan at the film edge (see the inset) is around ~0.9 nm. This larger value compared to theoretical thickness (0.33 nm) is a result of AFM cantilever tip effects including trapped water and gas molecules at the tip−surface interface.[36] Figure 2k shows a UV−Vis absorption spectrum and a corresponding Tauc plot (assuming a direct band gap[37]) acquired from a h-BN film transferred onto a sapphire substrate. A strong peak with a sharp absorption edge has been observed at 202 nm, corresponding to a band gap of around 6.03 eV as extracted from the Tauc plot.

Figure 3 provides a summary of data of growth directions of h-BN flakes. Three different growth directions have been observed, as marked in the SEM image shown in Figure 3a. The blue triangle marks a h-BN flake in the dominant growth direction designated as epitaxial-0°; the orange triangle marks a h-BN flake in the second preferable growth direction designated as epitaxial-180°; and the red circle marks a h-BN flake which is misoriented. Statistical analysis of the three growth directions is summarized in Figure 3b; 89% of the h-BN flakes have been grown in the epitaxial-0° direction, about 10.2% percent of the h-BN flakes have been grown in the

https://doi.org/10.1021/acsanm.1c00298
ACS Appl. Nano Mater. 2021, 4, 5685−5695

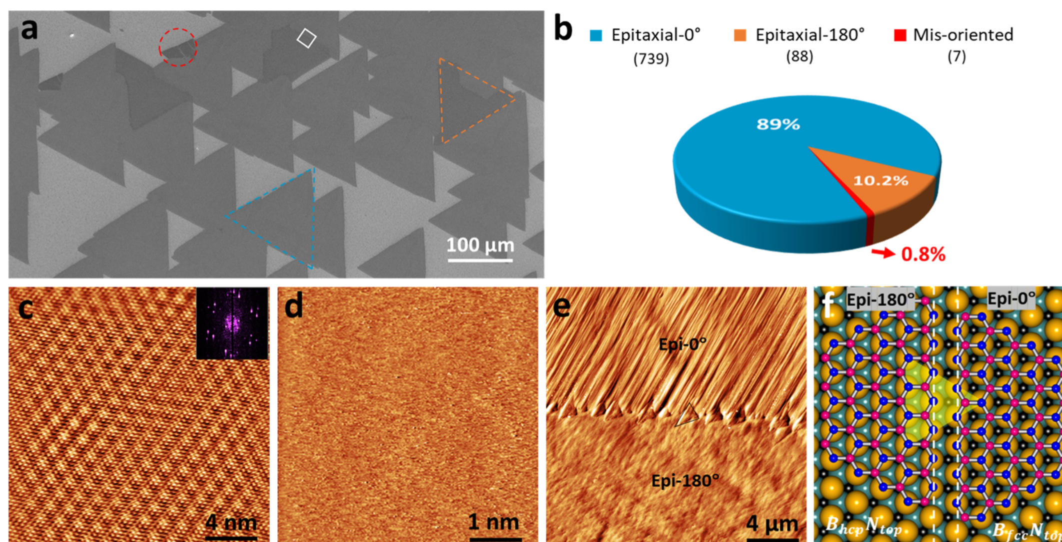

Figure 3. Analysis of h-BN growth orientations. (a) SEM image of h-BN flakes with different growth orientations. The blue and orange triangles and purple circles mark the epitaxial-0°, epitaxial-180°, and misoriented h-BN flakes, respectively; (b) statistical analysis of h-BN flakes with three different growth orientations; (c) STM image taken on the misoriented h-BN flake; (d) STM image taken on the epitaxial-0° flake; the inset shows the pattern after FFT transformation; (e) AFM image taken on the grain boundary between epitaxial-0° and epitaxial-180° flakes as marked with the white square in (a); and (f) atomic model of proposed configuration of the grain boundary.

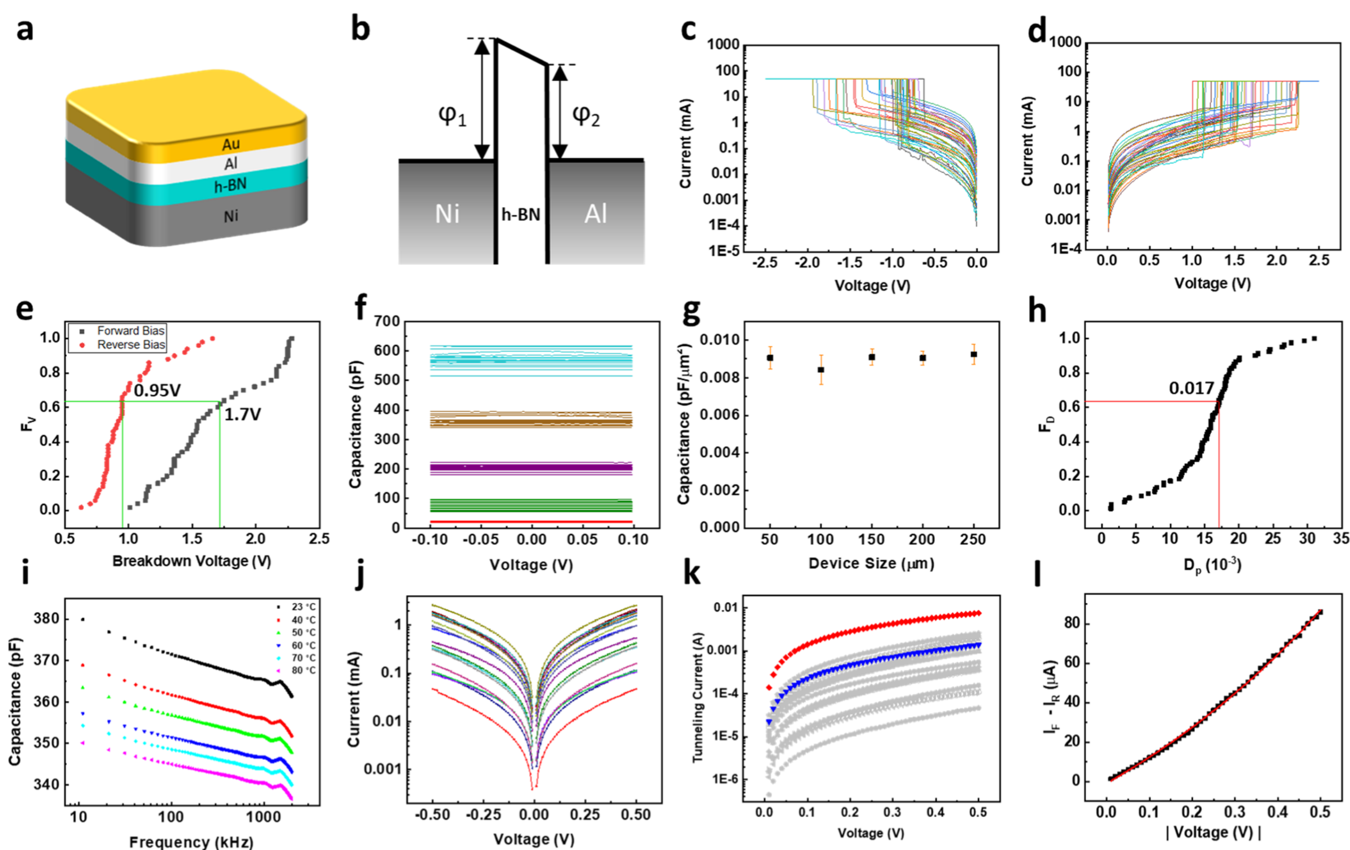

Figure 4. Characterization of nanocapacitors fabricated on the single-crystal h-BN film. (a) Model of capacitor's structure; (b) energy band diagram of the capacitor at thermal equilibrium; (c) reverse $I-V$ characteristics of 50 capacitors with the sweeping voltage reaching −2.5 V; (d) forward $I-V$ characteristics of 50 capacitors with the sweeping voltage reaching 2.5 V; (e) cumulative probability distribution of breakdown voltages; (f) $C-V$ characteristics at 1 MHz of 100 capacitors with the size of 50 × 50, 100 × 100, 150 × 150, 200 × 200, and 250 × 250 μm^2; (g) specific capacitance of capacitors with each size; (h) cumulative probability distribution of the dissipation factor of $C-V$ results shown in (f); (i) temperature-dependent frequency-dependent capacitance of a capacitor with a size of 200 × 200 μm^2; (j) tunneling currents of 20 capacitors with the size of 200 × 200 μm^2; (k) tunneling current with the calculated results colored in red (hole tunneling) and blue (electron tunneling) and experimental results colored in gray; and (l) plot of forward current minus reverse current ($i_F - i_R$) vs |voltage|.

https://doi.org/10.1021/acsanm.1c00298
ACS Appl. Nano Mater. 2021, 4, 5685−5695

epitaxial-180° direction, and only about 0.8% of the h-BN flakes have been misoriented. According to theoretical[10,32] and experimental[38] results, the epitaxial-0° orientation has the $B_{fcc}N_{top}$ configuration, and the epitaxial-180° orientation has the $B_{hcp}N_{top}$ configuration. The energy difference between these two epitaxial relationships led to a different number of flakes. Additional discussion of the growth mechanism is shown in Figure S4 in the Supporting Information section. The misoriented h-BN flakes are only observed around crystal defect sites or impurities over substrate surfaces. Figure 3c,d shows STM images taken on misoriented and epitaxial h-BN flakes, respectively. Moiré patterns have been obtained from misoriented flakes, while no features were resolved on epitaxial flakes. Note that the scanning tunneling microscope employed is a tabletop instrument, which can only be operated at room temperature and in the ambient environment, and the scanning tips are made from plier-cut Pt−Ir wires. Therefore, lateral and vertical resolutions are not as good to resolve the B or N atoms. Nevertheless, the relatively large features of the Moiré pattern on the misoriented flakes can be easily resolved. This result also confirms that there is no in-plane rotation between the epitaxial h-BN flakes and the Ni(111) surface. Figure 3e shows AFM images taken on the grain boundary between epitaxial-0° and epitaxial-180° h-BN flakes, marked by the white square, as shown in Figure 3a. As seen from the images, surface morphologies under epitaxial-0° and epitaxial-180° flakes are different: the surface under epitaxial-0° flakes is corrugated, while the surface under epitaxial-180° flakes is relatively flat. This difference in morphologies might have been caused by the different epitaxial relationships[39] and leads to different gray scale contrasts in the SEM image. The corrugated surface has a larger surface-to-volume ratio; therefore, many more secondary electrons have been generated; and in turn, the epitaxial-0° flakes look brighter than the epitaxial-180° flakes. Small h-BN adlayers are formed along the grain boundary, as marked by the black triangle, which are attributed to the intercalation growth at line defects.[32] Figure 3f shows a proposed atomic model at the grain boundary by assuming that all triangular h-BN flakes have N-terminated zigzag edges, and N will always sit on the top site.[40] When epitaxial-0° and epitaxial-180° h-BN flakes meet, a mismatch region is formed. According to the theoretical calculation,[41] instead of forming stable line defects, this type of mismatch will lead to a transition region, which opens up a channel for intercalation growth of h-BN adlayers. The yellow triangle illustrates the h-BN adlayers at the interface as observed in Figure 1e. The intercalated h-BN adlayers patch up the line defects, ensuring the insulating character of the h-BN film.

Figure 4 shows the electrical characterization results obtained from nanocapacitors fabricated on single-crystal h-BN films. A schematic of the capacitor structure is shown in Figure 4a, where the bottom electrode is the Ni(111) substrate. The top electrodes are square-shaped metal contacts fabricated by conventional photolithography and e-beam evaporation, which consist of 20 nm thick Al and 100 nm thick Au layers. The rationale for choosing Al as the top contact is as follows: as mentioned in the introduction section, h-BN films can be damaged by "high-energy" atoms evaporated from a hot metal surface. Because the energy possessed by evaporated atoms or a cluster is mainly from e-beam thermal heating, one way to diminish the damage on a target surface is to cool the hot atoms. Al can reach a high vapor pressure at a very low temperature of 821 °C under 10^{-6} Torr. In comparison, it takes Pt to reach 1492 °C, Ti to reach 1235 °C, and Ni to reach 1072 °C to attain the same vapor pressure (from Kurt J. Lesker, Inc.). Overall, evaporated Al atoms possess less energy at the same deposition rate. Furthermore, energy stored in the excitation states of commonly used heavy transition metals can be converted into kinetic energy upon reaching the surface, which possess much higher energy compared to lighter Al atoms.[42] As mentioned in the Introduction section, a similar strategy has been reported recently, where low-thermal-energy evaporation deposition of indium is employed to avoid damaging the MoS_2 film.[20]

Figure 4b shows the energy band diagram of capacitors at equilibrium, where φ_1 and φ_2 are the barrier heights of Ni/h-BN and Al/h-BN junctions, respectively. Due to the difference in the work function between Ni and Al, φ_1 is about 1 eV larger than φ_2 theoretically,[43] which results in a built-in potential across the h-BN layer. For convenience, the electrical characteristic will be described as "forward" when Ni is positively biased and as "reverse" when Al is positively biased. Figure 4c shows the reverse $I-V$ characteristics of 50 capacitors with the sweeping voltage reaching −2.5 V. Figure 4d shows the forward $I-V$ characteristics of 50 capacitors with the sweeping voltage reaching 2.5 V. The cumulative probability distribution of forward and reserve breakdown voltages is summarized in Figure 4e. By setting the probability to 0.63 according to the Weibull distribution,[44] we estimate the characteristic forward and reverse breakdown voltages to be 1.7, and 0.95 V, respectively, and the difference (0.85 V) is attributed to the built-in voltage at equilibrium.

Figure 4f shows $C-V$ characteristics of 100 capacitors with different sizes. The $C-V$ measurement was done with an Agilent E4980A precision LCR meter in the Cp-D mode at a frequency of 1 MHz, and the sweep range is from −0.1 to 0.1 V. Before measurement, the system is open/short corrected. Overall, the average capacitance value for different sizes is ~23 pF for devices with $50 \times 50\ \mu m^2$ (red), ~90 pF for devices with $100 \times 100\ \mu m^2$ (green), ~210 pF for devices with $150 \times 150\ \mu m^2$ (purple), ~363 pF for devices with $200 \times 200\ \mu m^2$ (brown), and ~580 pF for devices with $250 \times 250\ \mu m^2$ (blue). No discernible changes of capacitance are observed within the sweeping range. The specific capacitances of devices of all sizes are summarized in Figure 4g, and the average value is estimated to be 0.009 pF/μm^2. The cumulative probability distribution of the average dissipation factor of the devices is shown in Figure 4h. The characteristic value at a probability of 0.63 is 0.017. The dissipation factor shows no apparent relationship between voltage and device size within the measured range. The geometric configuration of the capacitor based on monolayer h-BN is shown in Figure S5. Due to the vdW interaction, an interface space exists between h-BN and metal electrodes, which is confirmed by both experimental[45,46] and theoretical[47] results. The h-BN/Ni separation is 2.12 Å and the h-BN/Al separation is 3.67 Å.[47] Therefore, the geometric distance between two electrodes can be estimated to be 5.79 Å, which consists of 3.33 Å of h-BN ($\varepsilon_r = 3.29$[35,48]) and 2.46 Å of a low-permittivity layer ($\varepsilon_r = 1$). The geometric capacitance (C_g) is the series capacitance of h-BN and the low permittivity layer, which can be calculated based on the following equation

$$C = \frac{\varepsilon_0 \varepsilon_r S}{d} \tag{1}$$

https://doi.org/10.1021/acsanm.1c00298
ACS Appl. Nano Mater. 2021, 4, 5685−5695

where ε_0 is the permittivity of free space, ε_r is the relative permittivity, S is the device area, and d is the dielectric thickness. The calculated geometric capacitance is 0.025 pF/μm^2. As a result, the measured capacitance at 1 MHz is only 36% of the geometric capacitance. A similar phenomenon was observed in capacitors fabricated with ferroelectric dielectric materials, which is attributed to the low permittivity "dead layer" formed at the ferroelectric−metal interface.[49,50] This low permittivity "dead layer" is related to the intrinsic properties of the bulky ferroelectric materials; thus, it should not be the reason for our case. It is reported that the Al thin film tends to form high contact resistance with graphene, which is attributed to the delamination of the Al thin film and penetration of oxygen into the interface.[51,52] However, it is not likely the reason for the smaller capacitance and good insulating property of our devices. If the smaller measured capacitance (C_m) compared to geometric capacitance (C_g) would have been caused by a series aluminum oxide (Al_2O_3) capacitance, the corresponding oxide layer would be as thick as 5.7 nm. It is impossible to form such a thick oxide layer at the Al/h-BN interface. Figure S6a,b shows the photo and optical microscopy image of patterned electrodes after lift-off with "acetone + sonication", indicating the robust contact of "20 nm Al + 100 nm Au" to h-BN. Depth-profiling XPS of the electrode shown in Figure S6c−h precludes any Al_2O_3 between metal and the h-BN film that would have been inadvertently formed.

To clarify this issue, we noted that for normal capacitors with thick dielectric materials, the contribution of quantum effects and uneven interfacial distance to the total capacitance is negligible. However, when the dielectric thickness goes down to the nanometer scale, their contribution should be considered.[53,54] The quantum capacitance (C_q) and "vacuum layer" capacitance (C_v) are considered in series with the geometric capacitance. Therefore

$$\frac{1}{C_m} = \frac{1}{C_g} + \frac{1}{C_q} + \frac{1}{C_v} \tag{2}$$

To eliminate the decrease of measured capacitance caused by dielectric dispersion, C_m used here is the average capacitance obtained at 200 Hz (Figure S7), and the value is 0.012 pF/μm^2. C_q is caused by penetration of the electric field into the electrodes and a decrease of electron energy states at the metal surface, the so-called Thomas−Fermi screening effect. C_q is defined as[53]

$$C_q = \frac{\varepsilon_m S}{2.3L} \tag{3}$$

where $L = \left(\frac{\varepsilon_m E_f}{2n_0 e^2}\right)^{1/2}$ is the Debye length; ε_m is the permittivity of metal, which equals the permittivity of free space (ε_0); E_f is the Fermi energy; and n_0 is the free electron density. Using the parameters of Al ($n_0 = 18.1 \times 10^{28}$ m^{-3}, E_f = 11.7 eV[55]), we can get L = 0.042 nm. The calculation based on Ni yields a similar result. However, due to the lower atomic density of deposited metal films, the free electron density might be lower on the Al side. Similarly, considering the large amount of B dissolved into the substrate during growth, the free electron density might also be reduced on the Ni side. Therefore, the actual value of L might be larger than 0.042 nm. For quantitative analysis, we chose the commonly recommended value for the Debye length, 0.05 nm,[53] and based on this value, C_q is 0.077 pF/μm^2. Substituting C_m, C_g, and C_q into eq 2 yields C_v of 0.033 pF/μm^2, and the corresponding effective vacuum layer thickness calculated based on eq 1 is 2.68 Å. The vacuum layer can be attributed to the corrugations of the h-BN film,[56,57] metal substrate surface reconstruction,[14,39] and crystallographic defects on metal contacts such as grain boundaries, atomic steps, and dislocations. The interface of the Al/h-BN stack was characterized using AFM, and the result is shown in Figure S8, where differences in the surface roughness would indicate the presence of vacuum gaps. An effective distance d^* between positive and negative charges accumulated in the capacitor thus can be estimated by summing up the geometric distance (5.79 Å), quantum layer thickness (2.3 L), and effective vacuum layer thickness (2.68 Å), which yields 9.62 Å.

Figure 4i shows the temperature-dependent C−f sweep on capacitors with the size of 200 × 200 μm^2. The sweeping frequency ranges from 10 kHz to 2 MHz, and the temperature ranges from room temperature to 80 °C. The capacitance decreases almost linearly with the increase of the temperature. The temperature capacitance coefficient (TCC) at 1 MHz is calculated using the following equation[58]

$$\mathrm{TCC} = \frac{\Delta C \times 10^6}{C \times \Delta T} \tag{4}$$

Using the capacitance at 23 °C as the reference, the TCC is calculated to be −1200 ppm/°C. The relationship between polarization P and relative permittivity ε_r can be expressed in the following equation[59]

$$P = P_e + P_i + P_d + P_s = \varepsilon_0(\varepsilon_r - 1)E \tag{5}$$

where P_e is electronic polarization, P_i is ionic polarization, P_d is dipolar polarization, and P_s is space charge polarization. The decrease of capacitance with the increase of temperature may be due to the decrease of electronic polarizability and the decrease in the number of polarizable electrons per unit volume according to the Clausius−Mossotti equation.[60] The capacitance decreases with the increase of frequency below 1 MHz, which may be attributed to the decrease of electronic polarizability, and the rapid decrease beyond 1 MHz may be attributed to the decrease of ionic polarizability.[59] However, even though a similar phenomenon has also been observed in tri-layer h-BN capacitors,[35] it is theoretically not allowed in materials with a small dielectric constant. While more investigation is required to understand the reason, we hypothesize that it is related to the interface interaction between monolayer h-BN and the metal electrode, especially between epitaxial h-BN and the Ni(111) substrate surface, which may render it very different to its bulk or free-standing state. For thick h-BN films where the contribution of interface interaction is negligible, there is no apparent dielectric loss observed below 3 MHz.[19]

Figure 4j shows the tunneling current characteristics of 20 capacitors, with the same size of 200 × 200 μm^2. For each capacitor, we perform the forward sweeping first and then perform the reverse sweeping. Curves with the same color are from the same devices. The tunneling current density between dissimilar electrodes is expressed with the Simmons equation (for $0 < V < \varphi_{min}/e$) given below[61]

$$J = \frac{e}{2\pi h d^2} \times [\bar{\varphi} \times e^{-4\pi d\sqrt{2m\bar{\varphi}}/h} - (\bar{\varphi} + eV) \times e^{-4\pi d\sqrt{2m(\bar{\varphi}+eV)}/h}] \tag{6}$$

https://doi.org/10.1021/acsanm.1c00298
ACS Appl. Nano Mater. 2021, 4, 5685−5695

where $\bar{\varphi} = (\varphi_1 + \varphi_2 - eV)/2$ is the average potential across the dielectric barrier, V is the applied voltage, e is the electron charge, m is tunneling carrier's mass, h is Planck's constant, and d is the tunneling distance. While some reports assumed that electrons are the tunneling carrier,[62,63] some other reports assumed holes as the tunneling carrier.[64,65] Obviously, which type of carrier is the tunneling carrier is still under debate, and more investigations are required to reach a conclusion. There are many factors contributing to the inconclusiveness. One of them originates from an uncertain estimation of the effective masses of the carriers. Most of the reports used $0.26m_0$ for effective electron mass and $0.5m_0$ for effective hole mass; both values are obtained from the paper of Xu and Ching.[66] While tunneling happens perpendicular to the 2D plane, these two values are the in-plane effective carrier masses. Nevertheless, according to studies by Xu and Ching,[66] "the effective mass for h-BN is highly anisotropic with average in-plane components a factor of 5 smaller than the components perpendicular to the plane". Specifically, as reported in ref 66, the out-of-plane effective electron mass is $2.21m_0$, and the out-of-plane effective hole mass is $1.33m_0$. For materials with apparent anisotropy, corresponding effective carrier masses in the tunneling direction should be used.[67,68] Thus, we will use out-of-plane effective masses in the calculations below.

Another parameter to determine is tunneling barriers for electrons and holes. Hattori et al. reported the Fermi level pinning effect at the h-BN interface when heavy transition metals are used.[65] In general, Fermi level pinning happens at the interface where a large amount of surface states exist, and it is usually related to defects at the dielectric/metal interface. For our monolayer h-BN MIM devices, it is unlikely that such a large amount of surface states would exist while maintaining a good insulating property. On the other hand, the Fermi level pinning observed in the multilayer h-BN MIM devices with heavy transition metals as electrodes indicate that the h-BN surface was damaged,[65] which supports our hypothesis that heavy transition metals can damage h-BN films during metallization. Moreover, the Fermi level pinning in MoS_2 MIM devices was avoided by electrode transfer and low-thermal-energy deposition of indium as mentioned above.[17,20] Similarly in our case, we believe that there is no Fermi level pinning because low-energy Al evaporation is employed. To the best of our knowledge, the absolute values of the barrier heights φ_1 and φ_2 have not been experimentally determined to date. It is reported that the barrier height in the Au/h-BN/AFM tip and Au/h-BN/Au configuration is about 3 eV, and the tunneling carrier is assumed to be electrons.[3,63] In our previous paper[13] and the references therein, the Schottky barrier between Ni/h-BN for electrons is 3.0 eV. Thus, to estimate the tunneling current, we assume that φ_1 equals 3 eV, the band gap of h-BN equals 6 eV,[37] the tunneling distance equals the geometric distance (5.79 Å), and the tunneling area is 200 μm × 200 μm. The tunneling current at 0.1 V would be 3.87 A, assuming that electrons are the tunneling carrier, and 10.8 A, assuming that holes are the tunneling carrier. Compared to the measured tunneling current (~0.3 mA at 0.1 V) shown in Figure 4j, the calculated results are about 4 orders of magnitude larger. This discrepancy originates from the fact that the actual tunneling area is different from the physical area of the device.[13] If we assume that tunneling only happens in some local areas, we can infer that the effective tunneling area is about 0.01% of the physical area of the devices, which is consistent with our previous report.[13] It should be noted that the Thomas−Fermi screen effect and the uneven interface distance were not considered in the abovementioned calculation. The justification is that tunneling has the highest probability at the locations with the thinnest barrier per quantum mechanics. On the other hand, if we assume an ideal case with the following two conditions, (1) tunneling happens all over the physical area of the devices and (2) the same effective distance (9.62 Å) obtained from the capacitance measurement/discussion applies to the entire physical area of the devices even if uneven interface distance is obvious across the device area, the electron tunneling current is estimated to be 0.23 mA, and the hole tunneling current is 1.41 mA at a bias of 0.1 V. The calculated tunneling currents versus applied voltages are plotted, as shown in Figure 4k. The hole current is colored in red, the electron current is colored in blue, and the experimental results shown in Figure 4j are colored in gray. The figure shows that both values are very close to the experimental results, especially the electron tunneling current, which lies within the range of our measured results. This situation prevents us from precisely determining which carrier is the dominating tunneling carrier. Based on the fact that the calculated electron tunneling current and hole tunneling current are not substantially different, although the hole current is larger than the electron current, we hypothesize that in the present h-BN MIM system with the monolayer h-BN film, both electrons and holes have participated in the tunneling process.

To study the relationship between the tunneling current and the bias polarity, we plotted the average difference between the forward and reverse currents versus the bias voltage, and the result is shown in Figure 4l. It turns out that the forward current is larger than the reverse current at the same bias. According to theoretical calculations, polarity-dependent tunneling should only appear when the applied bias is larger than one of the barrier heights, the so-called field emission region.[61,69] Our results show that even for the direct tunneling region, an asymmetric $I-V$ characteristic appears, and the difference in the tunneling current can be fitted well with the following equation

$$|i_{\text{Forward}}| - |i_{\text{Reverse}}| = A_1 \exp\left(-\frac{V}{t_1}\right) + A_2 \exp\left(-\frac{V}{t_2}\right) \quad (7)$$

where A_1, A_2, t_1, and t_2 are constants, and V is the applied voltage. This asymmetric $I-V$ relationship indicates that thermionic emission might have also contributed to the measured current.[70]

4. CONCLUSIONS

Monolayer single-crystal h-BN films with a size of 1 in.^{2} were synthesized on single-crystal Ni(111) substrates obtained by high-temperature annealing of Ni foils. By adopting an electropolishing procedure, the h-BN nucleation density and the growth speed increase significantly, and high-quality h-BN films could be obtained within 1 h. Robust nanocapacitors were fabricated on as-grown monolayer single-crystal h-BN films with Al as the top electrode. The tunneling current mechanism with asymmetric metal electrodes and the nanocapacitance effect were studied in detail. The effective distance, which is larger than the geometric dielectric thickness, was introduced based on theoretical and experimental analysis to explain the capacitances of the MIM nanocapacitors. Both electrons and holes may have been

tunneling carriers contributing to the tunneling currents. Our studies provide insights into quantum tunneling devices based on vdW materials. Finally, our experimental procedures are readily replicable, which provide a reliable method for developing practical devices based on monolayer single-crystal h-BN films.

■ ASSOCIATED CONTENT

Supporting Information

The Supporting Information is available free of charge at https://pubs.acs.org/doi/10.1021/acsanm.1c00298.

> Substrate preparation; XPS characterization of substrates; temperature-dependent growth; characterization of h-BN nuclei; schematic of an ideal capacitor with monolayer h-BN as dielectric; depth-profiling XPS of patterned electrodes; size-dependent low-frequency *C*−*f* profiles; and Al/h-BN interface morphology characterization (PDF)

■ AUTHOR INFORMATION

Corresponding Author

Jianlin Liu − *Department of Electrical and Computer Engineering, University of California, Riverside, California 92521, United States;* orcid.org/0000-0001-6513-0867; Phone: 1-9518277131; Email: jianlin@ece.ucr.edu; Fax: 1-9518272425

Authors

Yanwei He − *Department of Electrical and Computer Engineering, University of California, Riverside, California 92521, United States*

Yuan Li − *Department of Electrical and Computer Engineering, University of California, Riverside, California 92521, United States*

Miguel Isarraraz − *Department of Electrical and Computer Engineering, University of California, Riverside, California 92521, United States*

Pedro Pena − *Department of Chemistry, University of California, Riverside, California 92521, United States*

Jason Tran − *Department of Physics and Astronomy, University of California, Riverside, California 92521, United States*

Long Xu − *Department of Electrical and Computer Engineering, University of California, Riverside, California 92521, United States; School of Physical Science and Technology, Southwest University, Chongqing 400715, China;* orcid.org/0000-0002-3243-4087

Hao Tian − *Department of Electrical and Computer Engineering, University of California, Riverside, California 92521, United States;* orcid.org/0000-0001-5893-2319

Tianchen Yang − *Department of Electrical and Computer Engineering, University of California, Riverside, California 92521, United States*

Peng Wei − *Department of Physics and Astronomy, University of California, Riverside, California 92521, United States;* orcid.org/0000-0003-2289-6007

Cengiz S. Ozkan − *Materials Science and Engineering Program and Department of Mechanical Engineering, University of California, Riverside, California 92521, United States;* orcid.org/0000-0001-6751-6851

Mihrimah Ozkan − *Department of Electrical and Computer Engineering, University of California, Riverside, California 92521, United States*

Complete contact information is available at: https://pubs.acs.org/10.1021/acsanm.1c00298

Notes

The authors declare no competing financial interest.

■ ACKNOWLEDGMENTS

This work was supported by SHINES, an Energy Frontier Research Center (EFRC) funded by the US Department of Energy, The Office of Science, Basic Energy Sciences Division, under award #SC0012670, and by the UCR Academic Senate Committee on Research grant. J.T. and P.W. would also like to acknowledge NSF Convergence Accelerator Track C under award 2040620 and NSF QLCI-CG under award 1937155. The XPS data are obtained with support from NSF grant DMR-0958796.

■ REFERENCES

(1) Hattori, Y.; Taniguchi, T.; Watanabe, K.; Nagashio, K. Layer-by-Layer Dielectric Breakdown of Hexagonal Boron Nitride. *ACS Nano* **2015**, *9*, 916−921.

(2) Lee, G.-H.; Yu, Y.-J.; Cui, X.; Petrone, N.; Lee, C.-H.; Choi, M. S.; Lee, D.-Y.; Lee, C.; Yoo, W. J.; Watanabe, K.; Taniguchi, T.; Nuckolls, C.; Kim, P.; Hone, J. Flexible and Transparent MoS_2 Field-Effect Transistors on Hexagonal Boron Nitride-Graphene Heterostructures. *ACS Nano* **2013**, *7*, 7931−7936.

(3) Jang, S. K.; Youn, J.; Song, Y. J.; Lee, S. Synthesis and Characterization of Hexagonal Boron nitride As a Gate Dielectric. *Sci. Rep.* **2016**, *6*, 30449.

(4) Gupta, B.; Matte, H. S. S. R. Solution-Processed Layered Hexagonal Boron Nitride Dielectrics: A Route toward Fabrication of High Performance Flexible Devices. *ACS Appl. Electron. Mater.* **2019**, *1*, 2130−2139.

(5) Pan, C.; Ji, Y.; Xiao, N.; Hui, F.; Tang, K.; Guo, Y.; Xie, X.; Puglisi, F. M.; Larcher, L.; Miranda, E.; Jiang, L.; Shi, Y.; Valov, I.; McIntyre, P. C.; Waser, R.; Lanza, M. Coexistence of Grain-Boundaries-Assisted Bipolar and Threshold Resistive Switching in Multilayer Hexagonal Boron Nitride. *Adv. Funct. Mater.* **2017**, *27*, 1604811.

(6) Qian, K.; Tay, R. Y.; Nguyen, V. C.; Wang, J.; Cai, G.; Chen, T.; Teo, E. H. T.; Lee, P. S. Hexagonal Boron Nitride Thin Film for Flexible Resistive Memory Applications. *Adv. Funct. Mater.* **2016**, *26*, 2176−2184.

(7) Grosso, G.; Moon, H.; Lienhard, B.; Ali, S.; Efetov, D. K.; Furchi, M. M.; Jarillo-Herrero, P.; Ford, M. J.; Aharonovich, I.; Englund, D. Tunable and High-Purity Room Temperature Single-Photon Emission from Atomic Defects in Hexagonal Boron Nitride. *Nat. Commun.* **2017**, *8*, 705.

(8) Lee, J. S.; Choi, S. H.; Yun, S. J.; Kim, Y. I.; Boandoh, S.; Park, J.-H.; Shin, B. G.; Ko, H.; Lee, S. H.; Kim, Y.-M.; Lee, Y. H.; Kim, K. K.; Kim, S. M. Wafer-Scale Single-Crystal Hexagonal Boron Nitride Film via Self-Collimated Grain Formation. *Science* **2018**, *362*, 817−821.

(9) Wang, L.; Xu, X.; Zhang, L.; Qiao, R.; Wu, M.; Wang, Z.; Zhang, S.; Liang, J.; Zhang, Z.; Zhang, Z.; Chen, W.; Xie, X.; Zong, J.; Shan, Y.; Guo, Y.; Willinger, M.; Wu, H.; Li, Q.; Wang, W.; Gao, P.; Wu, S.; Zhang, Y.; Jiang, Y.; Yu, D.; Wang, E.; Bai, X.; Wang, Z.-J.; Ding, F.; Liu, K. Epitaxial Growth of a 100-Square-Centimetre Single-Crystal Hexagonal Boron Nitride Monolayer on Copper. *Nature* **2019**, *570*, 91−95.

(10) Chen, T.-A.; Chuu, C.-P.; Tseng, C.-C.; Wen, C.-K.; Wong, H.-S. P.; Pan, S.; Li, R.; Chao, T.-A.; Chueh, W.-C.; Zhang, Y.; Fu, Q.; Yakobson, B. I.; Chang, W.-H.; Li, L.-J. Wafer-Scale Single-Crystal

Hexagonal Boron Nitride Monolayers on Cu (111). *Nature* **2020**, *579*, 219−223.
(11) Zuo, Z.; Xu, Z.; Zheng, R.; Khanaki, A.; Zheng, J.-G.; Liu, J. In-itu Epitaxial Growth of Graphene/h-BN van der Waals Heterostructures by Molecular Beam Epitaxy. *Sci. Rep.* **2015**, *5*, 14760.
(12) Schmid, U. The Impact of Thermal Annealing and Adhesion Film Thickness on the Resistivity and the Agglomeration Behavior of Titanium/Platinum Thin Films. *J. Appl. Phys.* **2008**, *103*, 054902.
(13) Cui, Z.; He, Y.; Tian, H.; Khanaki, A.; Xu, L.; Shi, W.; Liu, J. Study of Direct Tunneling and Dielectric Breakdown in Molecular Beam Epitaxial Hexagonal Boron Nitride Monolayers Using Metal−Insulator−Metal Devices. *ACS Appl. Electron. Mater.* **2020**, *2*, 747−755.
(14) He, Y.; Tian, H.; Das, P.; Cui, Z.; Pena, P.; Chiang, I.; Shi, W.; Xu, L.; Li, Y.; Yang, T.; Isarraraz, M.; Ozkan, C. S.; Ozkan, M.; Lake, R. K.; Liu, J. Growth of High-Quality Hexagonal Boron Nitride Single-Layer Films on Carburized Ni Substrates for Metal−Insulator−Metal Tunneling Devices. *ACS Appl. Mater. Interfaces* **2020**, *12*, 35318−35327.
(15) Tian, H.; He, Y.; Das, P.; Cui, Z.; Shi, W.; Khanaki, A.; Lake, R. K.; Liu, J. Growth Dynamics of Millimeter-Sized Single-Crystal Hexagonal Boron Nitride Monolayers on Secondary Recrystallized Ni (100) Substrates. *Adv. Mater. Interfaces* **2019**, *6*, 1901198.
(16) Kim, C.; Lee, K. Y.; Moon, I.; Issarapanacheewin, S.; Yoo, W. J. Metallic Contact Induced van der Waals Gap in a MoS_2 FET. *Nanoscale* **2019**, *11*, 18246−18254.
(17) Liu, Y.; Guo, J.; Zhu, E.; Liao, L.; Lee, S.-J.; Ding, M.; Shakir, I.; Gambin, V.; Huang, Y.; Duan, X. Approaching the Schottky−Mott Limit in van der Waals Metal−Semiconductor Junctions. *Nature* **2018**, *557*, 696−700.
(18) Guo, N.; Wei, J.; Jia, Y.; Sun, H.; Wang, Y.; Zhao, K.; Shi, X.; Zhang, L.; Li, X.; Cao, A.; Zhu, H.; Wang, K.; Wu, D. Fabrication of Large Area Hexagonal Boron Nitride Thin Films for Bendable Capacitors. *Nano Res.* **2013**, *6*, 602−610.
(19) Ahmed, F.; Heo, S.; Yang, Z.; Ali, F.; Ra, C. H.; Lee, H.-I.; Taniguchi, T.; Hone, J.; Lee, B. H.; Yoo, W. J. Dielectric Dispersion and High Field Response of Multilayer Hexagonal Boron Nitride. *Adv. Funct. Mater.* **2018**, *28*, 1804235.
(20) Kim, B. K.; Kim, T. H.; Choi, D. H.; Kim, H.; Watanabe, K.; Taniguchi, T.; Rho, H.; Kim, J. J.; Kim, Y. H.; Bae, M. H. Origins of Genuine Ohmic van der Waals Contact Between Indium and MoS_2. *npj 2D Mater. Appl.* **2021**, *5*, 9.
(21) Bonifas, A. P.; McCreery, R. L. 'Soft'Au, Pt and Cu contacts for Molecular Junctions through Surface-Diffusion-Mediated Deposition. *Nat. Nanotechnol.* **2010**, *5*, 612−617.
(22) Haick, H.; Ambrico, M.; Ghabboun, J.; Ligonzo, T.; Cahen, D. Contacting Organic Molecules by Metal Evaporation. *Phys. Chem. Chem. Phys.* **2004**, *6*, 4538−4541.
(23) Nakhaie, S.; Wofford, J. M.; Schumann, T.; Jahn, U.; Ramsteiner, M.; Hanke, M.; Lopes, J. M. J.; Riechert, H. Synthesis of Atomically Thin Hexagonal Boron Nitride Films on Nickel Foils by Molecular Beam Epitaxy. *Appl. Phys. Lett.* **2015**, *106*, 213108.
(24) Shi, Y.; Hamsen, C.; Jia, X.; Kim, K. K.; Reina, A.; Hofmann, M.; Hsu, A. L.; Zhang, K.; Li, H.; Juang, Z.-Y.; Dresselhaus, M. S.; Li, L.-J.; Kong, J. Synthesis of Few-Layer Hexagonal Boron Nitride Thin Film by Chemical Vapor Deposition. *Nano Lett.* **2010**, *10*, 4134−4139.
(25) Ferguson, J. D.; Weimer, A. W.; George, S. M. Atomic Layer Deposition of Boron Nitride Using Sequential Exposures of BCl_3 and NH_3. *Thin Solid Films* **2002**, *413*, 16−25.
(26) Esfahani, A. N.; Malcolm, A. J.; Xu, L.; Yang, H.; Storwick, T.; Kim, N. Y.; Pope, M. A. Ultra-Thin Films of Solution-Exfoliated Hexagonal Boron Nitride by Langmuir Deposition. *J. Mater. Chem. C* **2020**, *8*, 13695−13704.
(27) Zhu, J.; Kang, J.; Kang, J.; Jariwala, D.; Wood, J. D.; Seo, J.-W. T.; Chen, K.-S.; Marks, T. J.; Hersam, M. C. Solution-Processed Dielectrics Based on Thickness-Sorted Two-Dimensional Hexagonal Boron Nitride Nanosheets. *Nano Lett.* **2015**, *15*, 7029−7036.
(28) Tian, H.; Khanaki, A.; Das, P.; Zheng, R.; Cui, Z.; He, Y.; Shi, W.; Xu, Z.; Lake, R.; Liu, J. Role of Carbon Interstitials in Transition Metal Substrates on Controllable Synthesis of High-Quality Large-Area Two-Dimensional Hexagonal Boron Nitride Layers. *Nano Lett.* **2018**, *18*, 3352−3361.
(29) Khanaki, A.; Tian, H.; Xu, Z.; Zheng, R.; He, Y.; Cui, Z.; Yang, J.; Liu, J. Effect of High Carbon Incorporation in Co Substrates on the Epitaxy of Hexagonal Boron Nitride/Graphene Heterostructures. *Nanotechnology* **2017**, *29*, 035602.
(30) Okazawa, T.; Nishizawa, T.; Nishimura, T.; Kido, Y. Oxidation Kinetics for Ni (111) and the Structure of the Oxide Layers. *Phys. Rev. B: Condens. Matter Mater. Phys.* **2007**, *75*, 033413.
(31) Huda, M. N.; Kleinman, L. H-BN Monolayer Adsorption on the Ni (111) Surface: A Density Functional Study. *Phys. Rev. B: Condens. Matter Mater. Phys.* **2006**, *74*, 075418.
(32) Grad, G.; Blaha, P.; Schwarz, K.; Auwärter, W.; Greber, T. Density Functional Theory Investigation of the Geometric and Spintronic Structure of h-BN/Ni (111) in View of Photoemission and STM Experiments. *Phys. Rev. B: Condens. Matter Mater. Phys.* **2003**, *68*, 085404.
(33) He, Y.; Tian, H.; Khanaki, A.; Shi, W.; Tran, J.; Cui, Z.; Wei, P.; Liu, J. Large-Area Adlayer-Free Single-Layer h-BN Film Achieved by Controlling Intercalation Growth. *Appl. Surf. Sci.* **2019**, *498*, 143851.
(34) Gorbachev, R. V.; Riaz, I.; Nair, R. R.; Jalil, R.; Britnell, L.; Belle, B. D.; Hill, E. W.; Novoselov, K. S.; Watanabe, K.; Taniguchi, T.; Geim, A. K.; Blake, P. Hunting for Monolayer Boron Nitride: Optical and Raman Signatures. *Small* **2011**, *7*, 465−468.
(35) Hong, S.; Lee, C.-S.; Lee, M.-H.; Lee, Y.; Ma, K. Y.; Kim, G.; Yoon, S. I.; Ihm, K.; Kim, K.-J.; Shin, T. J.; Kim, S. W.; Jeon, E.-c.; Jeon, H.; Kim, J.-Y.; Lee, H.-I.; Lee, Z.; Antidormi, A.; Roche, S.; Chhowalla, M.; Shin, H.-J.; Shin, H. S. Ultralow-Dielectric-Constant Amorphous Boron Nitride. *Nature* **2020**, *582*, 511−514.
(36) Khan, M.; Huang, Z.; Xiao, F.; Casillas, G.; Chen, Z.; Molino, P. J.; Liu, H. K. Synthesis of Large and Few Atomic Layers of Hexagonal Boron Nitride on Melted Copper. *Sci. Rep.* **2015**, *5*, 9547.
(37) Elias, C.; Valvin, P.; Pelini, T.; Summerfield, A.; Mellor, C.; Cheng, T.; Eaves, L.; Foxon, C.; Beton, P.; Novikov, S. Direct Band-Gap Crossover in Epitaxial Monolayer Boron Nitride. *Nat. Commun.* **2019**, *10*, 2639.
(38) Auwärter, W.; Muntwiler, M.; Osterwalder, J.; Greber, T. Defect Lines and Two-Domain Structure of Hexagonal Boron Nitride Films on Ni (1 1 1). *Surf. Sci.* **2003**, *545*, L735−L740.
(39) Fernández, L.; Makarova, A. A.; Laubschat, C.; Vyalikh, D. V.; Usachov, D. Y.; Ortega, J. E.; Schiller, F. Boron Nitride Monolayer Growth on Vicinal Ni (111) Surfaces Systematically Studied with a Curved Crystal. *2D Mater.* **2019**, *6*, 025013.
(40) Liu, S.; Van Duin, A. C. T.; Van Duin, D. M.; Liu, B.; Edgar, J. H. Atomistic Insights into Nucleation and Formation of Hexagonal Boron Nitride on Nickel from First-Principles-Based Reactive Molecular Dynamics Simulations. *ACS Nano* **2017**, *11*, 3585−3596.
(41) Park, H. J.; Cha, J.; Choi, M.; Kim, J. H.; Tay, R. Y.; Teo, E. H. T.; Park, N.; Hong, S.; Lee, Z. One-Dimensional Hexagonal Boron Nitride Conducting Channel. *Sci. Adv.* **2020**, *6*, No. eaay4958.
(42) Asano, T.; Uetake, N.; Suzuki, K. Mean Atomic Velocities of Uranium, Titanium and Copper during Electron Beam Evaporation. *J. Nucl. Sci. Technol.* **1992**, *29*, 1194−1200.
(43) Derry, G. N.; Kern, M. E.; Worth, E. H. Recommended Values of Clean Metal Surface Work Functions. *J. Vac. Sci. Technol., A* **2015**, *33*, 060801.
(44) Chauvet, C.; Laurent, C. Weibull Statistics in Short-Term Dielectric Breakdown of Thin Polyethylene Films. *IEEE Trans. Electr. Insul.* **1993**, *28*, 18−29.
(45) Yang, Y.; Fu, Q.; Li, H.; Wei, M.; Xiao, J.; Wei, W.; Bao, X. Creating a Nanospace under an h-BN Cover for Adlayer Growth on Nickel (111). *ACS Nano* **2015**, *9*, 11589−11598.
(46) Brülke, C.; Heepenstrick, T.; Humberg, N.; Krieger, I.; Sokolowski, M.; Weiß, S.; Tautz, F. S.; Soubatch, S. Long Vertical Distance Bonding of the Hexagonal Boron Nitride Monolayer on the Cu (111) Surface. *J. Phys. Chem. C* **2017**, *121*, 23964−23973.

https://doi.org/10.1021/acsanm.1c00298
ACS Appl. Nano Mater. 2021, 4, 5685−5695

(47) Bokdam, M.; Brocks, G.; Katsnelson, M. I.; Kelly, P. J. Schottky Barriers at Hexagonal Boron Nitride/Metal Interfaces: A First-Principles Study. *Phys. Rev. B: Condens. Matter Mater. Phys.* **2014**, *90*, 085415.
(48) Laturia, A.; Van de Put, M. L.; Vandenberghe, W. G. Dielectric Properties of Hexagonal Boron Nitride and Transition Metal Dichalcogenides: from Monolayer to Bulk. *npj 2D Mater. Appl.* **2018**, *2*, 6.
(49) Stengel, M.; Spaldin, N. A. Origin of the Dielectric Dead Layer in Nanoscale Capacitors. *Nature* **2006**, *443*, 679−682.
(50) Chang, L.-W.; Alexe, M.; Scott, J. F.; Gregg, J. M. Settling the "Dead Layer" Debate in Nanoscale Capacitors. *Adv. Mater.* **2009**, *21*, 4911−4914.
(51) Robinson, J. A.; LaBella, M.; Zhu, M.; Hollander, M.; Kasarda, R.; Hughes, Z.; Trumbull, K.; Cavalero, R.; Snyder, D. Contacting Graphene. *Appl. Phys. Lett.* **2011**, *98*, 053103.
(52) Miyazaki, H.; Li, S.; Kanda, A.; Tsukagoshi, K. Resistance Modulation of Multilayer Graphene Controlled by the Gate Electric Field. *Semicond. Sci. Technol.* **2010**, *25*, 034008.
(53) Ku, H. Y.; Ullman, F. G. Capacitance of Thin Dielectric Structures. *J. Appl. Phys.* **1964**, *35*, 265−267.
(54) Chkhartishvili, L.; Beridze, M.; Dekanosidze, S.; Esiava, R.; Kalandadze, I.; Mamisashvili, N.; Tabatadze, G. How to Calculate Nanocapacitance. *Am. J. Nano Res. Appl.* **2017**, *5*, 9−12.
(55) Ashcroft, N. W.; Mermin, N. D. *Solid State Physics*; Saunders College: Philadelphia, 1976;. Appendix N 2010, 166.
(56) Schwarz, M.; Riss, A.; Garnica, M.; Ducke, J.; Deimel, P. S.; Duncan, D. A.; Thakur, P. K.; Lee, T.-L.; Seitsonen, A. P.; Barth, J. V.; Allegretti, F.; Auwärter, W. Corrugation in the Weakly Interacting Hexagonal-BN/Cu (111) System: Structure Determination by Combining Noncontact Atomic Force microscopy and X-ray Standing Waves. *ACS Nano* **2017**, *11*, 9151−9161.
(57) de Lima, L. H.; Greber, T.; Muntwiler, M. The True Corrugation of a h-BN Nanomesh Layer. *2D Mater.* **2020**, *7*, 035006.
(58) Freire, F. N. A.; Santos, M. R. P.; Pereira, F. M. M.; Sohn, R. S. T. M.; Almeida, J. S.; Medeiros, A. M. L.; Sancho, E. O.; Costa, M. M.; Sombra, A. S. B. Studies of the Temperature Coefficient of Capacitance (TCC) of a New Electroceramic Composite: Pb-$(Fe_{0.5}Nb_{0.5})O_3$(PFN)−$Cr_{0.75}Fe_{1.25}O_3$(CRFO). *J. Mater. Sci.: Mater. Electron.* **2009**, *20*, 149−156.
(59) Badr, A. M.; Elshaikh, H. A.; Ashraf, I. M. Impacts of Temperature and Frequency on the Dielectric Properties for Insight into the Nature of the Charge Transports in the Tl_2S Layered Single Crystals. *J. Mod. Phys.* **2011**, *2*, 12.
(60) Cockbain, A. G.; Harrop, P. J. The Temperature Coefficient of Capacitance. *J. Phys. D: Appl. Phys.* **1968**, *1*, 1109.
(61) Simmons, J. G. Electric Tunnel Effect between Dissimilar Electrodes Separated by a Thin Insulating Film. *J. Appl. Phys.* **1963**, *34*, 2581−2590.
(62) Iqbal, M. Z.; Faisal, M. M. Fowler-Nordheim Tunneling Characteristics of Graphene/hBN/Metal Heterojunctions. *J. Appl. Phys.* **2019**, *125*, 084902.
(63) Lee, G.-H.; Yu, Y.-J.; Lee, C.; Dean, C.; Shepard, K. L.; Kim, P.; Hone, J. Electron Tunneling through Atomically Flat and Ultrathin Hexagonal Boron Nitride. *Appl. Phys. Lett.* **2011**, *99*, 243114.
(64) Britnell, L.; Gorbachev, R. V.; Jalil, R.; Belle, B. D.; Schedin, F.; Katsnelson, M. I.; Eaves, L.; Morozov, S. V.; Mayorov, A. S.; Peres, N. M. R.; Castro Neto, A. H.; Leist, J.; Geim, A. K.; Ponomarenko, L. A.; Novoselov, K. S. Electron Tunneling through Ultrathin Boron Nitride Crystalline Barriers. *Nano Lett.* **2012**, *12*, 1707−1710.
(65) Hattori, Y.; Taniguchi, T.; Watanabe, K.; Nagashio, K. Determination of Carrier Polarity in Fowler−Nordheim Tunneling and Evidence of Fermi Level Pinning at the Hexagonal Boron Nitride/Metal Interface. *ACS Appl. Mater. Interfaces* **2018**, *10*, 11732−11738.
(66) Xu, Y.-N.; Ching, W. Y. Electronic, Optical, and Structural Properties of Some Wurtzite Crystals. *Phys. Rev. B: Condens. Matter Mater. Phys.* **1993**, *48*, 4335.
(67) Ilatikhameneh, H.; Ameen, T.; Novakovic, B.; Tan, Y.; Klimeck, G.; Rahman, R. Saving Moore's Law Down to 1 nm Channels with Anisotropic Effective Mass. *Sci. Rep.* **2016**, *6*, 31501.
(68) Robbins, M. C.; Golani, P.; Koester, S. J. Right-Angle Black Phosphorus Tunneling Field Effect Transistor. *IEEE Electron Device Lett.* **2019**, *40*, 1988−1991.
(69) Banerjee, S.; Zhang, P. A Generalized Self-Consistent Model for Quantum Tunneling Current in Dissimilar Metal-Insulator-Metal Junction. *AIP Adv.* **2019**, *9*, 085302.
(70) Simmons, J. G. Potential Barriers and Emission-Limited Current Flow Between Closely Spaced Parallel Metal Electrodes. *J. Appl. Phys.* **1964**, *35*, 2472−2481.

https://doi.org/10.1021/acsanm.1c00298
ACS Appl. Nano Mater. 2021, 4, 5685−5695